(1941); R. Kronig, J. De Boer, J. Korringa, *Physica* XII, 245 (1946); D. J. Stevenson, *Nature* **268**, 130 (1977); Y. Fukai, *ibid.* **308**, 174 (1984).
14. Hydrogen was loaded into the diamond cell with T301 stainless steel gaskets at a pressure of 0.2 GPa [A. P. Jephcoat, H. K. Mao, P. M. Bell, in *Hydrothermal Experimental Techniques*, G. C. Ulmer and H. L. Barnes, Eds. (Wiley, New York, 1987), p. 469]. Pressure measurements were performed using ruby fluorescence; the R_1-R_2 splitting was well resolved up to 32 GPa [H. K. Mao, J. Xu, P. M. Bell, *J. Geophys. Res. B* **91**, 4673 (1986)].
15. H. K. Mao and P. M. Bell, *Science* **203**, 1004 (1979).
16. H. K. Mao, W. A. Bassett, T. Takahashi, *J. Appl. Phys.* **38**, 272 (1967).
17. Antonov *et al.* obtained indirect evidence for a reaction between iron and hydrogen at 3.5 GPa from electrical resistivity measurements (*8*).
18. J. V. Badding, H. K. Mao, R. J. Hemley, *Solid State Comm.* 77, 801 (1990).
19. C. Meade and R. Jeanloz, *Rev. Sci. Instrum.* **61**, 2571 (1990).
20. A. D. Mighell, C. R. Hubbard, J. K. Stalick, M. A. Holomany, *BookNBS*AIDS83: A Manual Describing the Data Format Used in NBS*AIDS83* (JCPDS-International Centre for Diffraction Data, Swarthmore, PA, 1983); the figure of merit for the fit ranged from 13 to 23. Peak positions were determined by a fit to a pseudo-Voight line profile [L. W. Finger, in *Reviews in Mineralogy*, D. L. Bish and J. E. Post, Eds. (Mineralogical Society of America, Washington, DC, 1989), vol. 20, p. 309].
21. The accuracy of intensity measurements in the diamond cell can be limited by preferred orientation, which is often observed because the small sample size can make it difficult to sample a truly random set of diffraction planes [H. K. Mao *et al.*, *Phys. Rev. Lett.* **64**, 1749 (1990)].
22. I. Choe, R. Ingalls, J. M. Brown, Y. Sato-Sorensen, R. Mills, *Phys. Rev. B*, in press.
23. H. K. Mao *et al.*, *Science* **239**, 1131 (1988).
24. H. K. Mao, Y. Wu, L. C. Chen, J. F. Shu, A. P. Jephcoat, *J. Geophys. Res. B* **95**, 21737 (1990).
25. F. E. Fujita, in *Hydrogen Degradation of Ferrous Alloys*, R. A. Oriani, J. P. Hirth, M. Smialowski, Eds. (Noyes, Park Ridge, NJ, 1985), pp. 1–14.
26. Although pressures of 0.2 GPa are insufficient to form bulk hydride, hydrogen can become trapped in cracks and voids where its fugacity can be increased by high local stresses, which will enhance its concentration locally in the surrounding steel [C. A. Wert, in *Hydrogen in Metals II*, G. Alefeld and J. Völkl, Eds. (Springer-Verlag, New York, 1978), pp. 305–328; H. P. van Leeuwen, in *Hydrogen Degradation of Ferrous Alloys*, R. A. Oriani, J. P. Hirth, M. Smialowski, Eds. (Noyes, Park Ridge, NJ, 1985), pp. 17–23]. It is difficult to directly probe the properties of metals near cracks and voids and the mechanism of embrittlement is poorly understood; bulk high pressure measurements such as those presented here can be used to determine the properties of ferrous hydrides or ferrous metals with high levels of hydrogen doping and aid our understanding of embrittlement.
27. R. J. Hemley and H. K. Mao, *Science* **249**, 391 (1990).
28. V. E. Antonov *et al.*, *Dokl. Akad. Nauk SSSR* **269**, 617 (1983); E. G. Ponyatovskii and V. E. Antonov, in *Problems in Solid-State Physics*, A. M. Prokhorov and A. S. Prokhorov, Eds. (MIR, Moscow, 1984), p. 109.
29. R. Jeanloz, *Annu. Rev. Earth Planet Sci.* **18**, 357 (1990).
30. A. Jephcoat and P. Olson, *Nature* **325**, 332 (1987).
31. J. V. Badding, H. K. Mao, R. J. Hemley, in preparation.
32. P. Vinet, J. Ferrante, J. Smith, J. H. Rose, *J. Phys. C* **19**, L467 (1986).
33. We thank C. Meade, L. W. Finger, R. E. Cohen, R. Jeanloz, and J. M. Brown for valuable discussions and comments on the manuscript. This work was supported by the National Science Foundation under grants EAR-8904080, EAR-8720320, and DMR-8912226 and the Carnegie Institution of Washington.

9 May 1991; accepted 12 June 1991

Commensurability and Mobility in Two-Dimensional Molecular Patterns on Graphite

JÜRGEN P. RABE* AND STEFAN BUCHHOLZ

Two-dimensional molecular patterns were obtained by the adsorption of long-chain alkanes, alcohols, fatty acids, and a dialkylbenzene from organic solutions onto the basal plane of graphite. In situ scanning tunneling microscopy (STM) studies revealed that these molecules organize in lamellae with the extended alkyl chains oriented parallel to a lattice axis within the basal plane of graphite. The planes of the carbon skeletons, however, can be oriented either predominantly perpendicular to or predominantly parallel with the substrate surface, causing the lamellar lattice to be either in or near registry with the substrate (alkanes and alcohols) or not in registry (fatty acids and dialkylbenzenes). In the case of the alcohols and the dialkylbenzene the molecular axes are tilted by +30° or −30° with respect to an axis normal to the lamella boundaries, giving rise to molecularly well-defined domain boundaries. Fast STM image recording allowed the spontaneous switch between the two tilt angles to be observed in the alcohol monolayers on a time scale of a few milliseconds.

ORGANIC MONOLAYERS OF MOLECular thickness play an important role in many interfacial phenomena, including wetting, lubrication and adhesion, and molecular and biological recognition. In addition, well-defined monolayers on inert supports are suitable model systems for the investigation of two-dimensional (2-D) phenomena. Because of a lack of true crystallinity in two dimensions, their in-plane structure remains, however, a challenge for both theory and experiment. For rare gas atoms under ultrahigh vacuum and at low temperatures, scattering methods have been successfully used to elucidate their typical 2-D behavior (*1*). Langmuir-Blodgett layers have also been investigated using, for example, electron scattering (*2*), x-ray scattering (*3, 4*), and Raman scattering methods (*5*), both in vacuum or under ambient conditions. With the help of STM (*6, 7*) it has become possible to directly observe structure and dynamics at solid-fluid interfaces in situ on the relevant length scales, that is, from the atomic scale to the micrometer scale and larger. In particular, STM images provide detailed information on the commensurability between molecular adsorbate and substrate lattices. A related issue, the mobility within the monolayer, can be observed by STM on a time scale of a few milliseconds (7). We demonstrate the cooperative reorientation in nanometer-size domains in a 2-D polycrystal. Information of this kind may improve our understanding of the mechanisms underlying various interfacial processes, including boundary lubrication, and may help in the development of theoretical models for molecular dynamics simulations of molecular monolayers. Finally, our increasing ability to characterize these systems will be important for efforts to generate a 2-D molecular patterns (*8*) on the submicrometer scale approaching nanometer dimensions. The latter may eventually prove useful for information storage.

Adsorption isotherms and enthalpies of adsorption (*9–11*) indicate that long-chain alkanes, alcohols, fatty acids, and alkylbenzenes adsorb as monomolecular layers from nonpolar organic solvents to the basal plane of graphite. However, there has been debate about whether the alkane adsorption is driven by the registry between the carbon lattices of adsorbate and substrate (*9*) or by a 2-D crystallization of the adsorbate on a flat substrate, independent of the substrate lattice (*10*). We present a detailed analysis of the order in monolayers of simple long-chain alkyl derivatives physisorbed at room temperature at the interface between the basal plane of graphite and an organic solution. It shows, in particular, the difference in registry in the directions parallel with and perpendicular to the alkane chains.

In order to observe nonconducting molecular adsorbates by STM, it is necessary that the adsorbate modifies the tunneling current sufficiently. This modification may be caused either by a change of the tunneling barrier (*12–15*) or by a change in the density of states within substrate or tip, due to their electronic interaction with the adsorbate (*16, 17*). In any case the image contrast depends on the tunneling bias. If under certain bias conditions the adsorbate modifies the tunneling current strongly, the image will be dominated by the adsorbate; if the modification is weak, the image will be dominated by the substrate. Particularly interesting for structure analysis is the case in which the image contains information about both substrate and adsorbate structure si-

Max-Planck-Institut für Polymerforschung, Postfach 3148, D-6500 Mainz, Germany.

*To whom correspondence should be addressed.

multaneously. Unfortunately, for organic adsorbates on metal substrates this is difficult to achieve without disrupting the adsorbate layer (*12, 16*). Part of the reason is that in these cases the interaction between adsorbate and substrate is relatively strong. Although this helps to immobilize molecules, it also makes it difficult to separate substrate and adsorbate properties. Physisorbed molecular monolayers on graphite, on the other hand, provide the opportunity to image the molecules with a minimum of substrate perturbation. Moreover, one can determine the commensurability between adsorbate and substrate lattices very accurately.

The STM was home-built (*18*). Highly oriented pyrolytic graphite (HOPG, Union Carbide, quality ZYB) was first carefully characterized under ambient conditions as well as in various solvents, in order to be able to unambiguously differentiate between defects in graphite [including $\sqrt{3} \times \sqrt{3}$ R30° superstructures around localized surface structures (*18*)] and images of the adsorbates. Adsorbed monolayers must be reproducibly imaged on large areas of the sample surface, and different tips and different substrate pieces must be used. Moreover, the images of monolayers from molecules of homologous series should be related. In situ STM imaging was performed at the internal interface between HOPG and concentrated but not saturated solutions of about ten alkanes with chain lengths ranging from nonadecane ($C_{19}H_{40}$) through pentacontane ($C_{50}H_{102}$); fatty acids including stearic acid ($C_{17}H_{35}COOH$), arachidic acid ($C_{19}H_{39}COOH$), and tetracosanoic acid ($C_{23}H_{47}COOH$); alcohols such as octadecanol ($C_{18}H_{37}OH$), tetracosanol ($C_{24}H_{49}OH$), and triacontanol ($C_{30}H_{61}OH$); and didodecylbenzene [$H_{25}C_{12}(C_6H_4)C_{12}H_{25}$] dissolved in phenyloctane, as described before (*19*). In some cases (*19*), we used different solvents such as diphenyl sulfide and 1,3,5-trimethyl-1,1,3,5,5-pentaphenyltrisiloxane for comparison and obtained the same results. We used Pt/Ir tips, which were prepared either mechanically or electrochemically and often conditioned in situ by short bias pulses. All of the images presented were obtained at quasi-constant height in the variable current mode. No digital image processing has been performed. The average current was set to 1 nA and the tip bias was about +1 V. These are tunneling conditions under which the STM images generally show contributions of both substrate and adsorbate simultaneously. However, the contrast also depends on the particular tip condition.

In Fig. 1 STM images of four representatives of the above-mentioned materials are shown. They are characteristic for their respective homologous series, but we limit ourselves here to the discussion of these particular cases. The images are typically found on areas larger than the scan range of

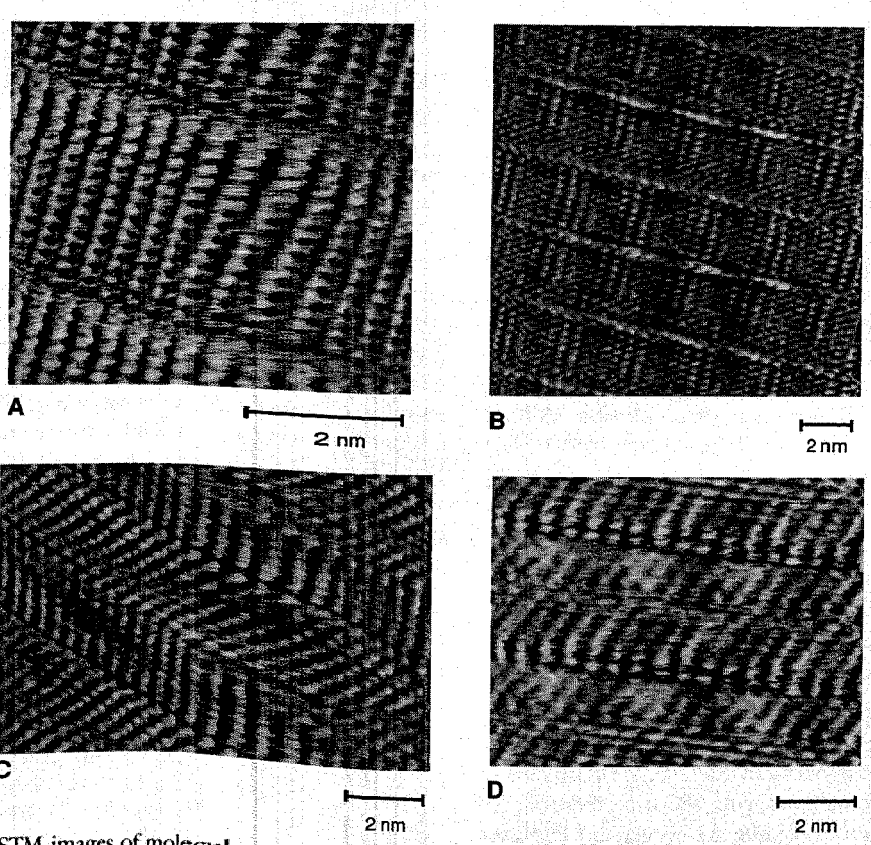

Fig. 1. STM images of molecular monolayers adsorbed to the basal plane of graphite. (**A**) The alkane heptacosane ($C_{27}H_{56}$); (**B**) the fatty acid stearic acid ($C_{17}H_{35}COOH$); (**C**) the alcohol octadecanol ($C_{18}H_{37}OH$); and (**D**) didodecylbenzene [$H_{25}C_{12}(C_6H_4)C_{12}H_{25}$]. The brightness is proportional to the current at quasi-constant height. The four cases show alkyl chains perpendicular to (A and B) and tilted (C and D) relative to the lamella boundaries (first and second row), as well as chain packings commensurate (A and C) and noncommensurate (B and D) with the substrate lattice (first and second column).

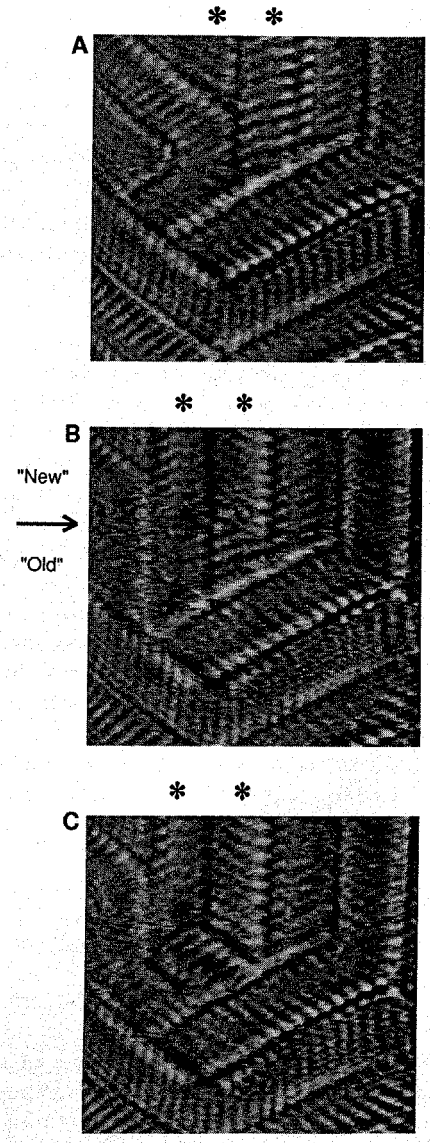

Fig. 2. STM images of a monolayer of octadecanol on graphite. The time elapsed between images (**A**) and (**C**) is a few seconds. Image (**B**) shows that the tilt direction of the molecules in the two vertical lamellae (*) at the upper left part of the image flips while the image is scanned from bottom to top. The line that was recorded when the flip occurred is marked by an arrow. From the sharpness of the transition and the scanning speed it can be concluded that the switching time is less than 10 ms. Note the stability of the surrounding herringbone structures with their molecularly well-defined domain boundaries. Image size: 11.7 nm × 11.0 nm.

1.5 μm. In addition, characteristic domain boundaries are observed [(*7, 19*) and Fig. 2]. All images displayed in Fig. 1 exhibit highly ordered lamellae. The sizes of the unit cells indicate that the lamellae consist of molecules that are extended and oriented parallel to the substrate. Although in the case of the alkane and the fatty acid the alkyl chains are oriented perpendicular to the lamella boundaries (Fig. 1, A and B), they are tilted in the case of the alcohol and the dialkylbenzene (Fig. 1, C and D). The comparison with the STM image of the graphite substrate before adsorption reveals that the molecular axes are oriented parallel to a carbon chain in graphite. This interpretation of the alkane image (Fig. 1A) agrees with the results of a recent report on another long-chain alkane, dotriacontane ($C_{32}H_{66}$) (*20*). However, as far as the registry between the adsorbate and substrate as well as the orientation of the planes of the carbon skeleton relative to the graphite surface are concerned, the following analysis leads to different conclusions.

Since we attribute the images to the structures of both substrate and adsorbate, the details must be due to the relative orientation of their lattices. Closer inspection of Fig. 1A reveals a small but distinct modulation of the contrast perpendicular to the lamella boundary, repetitive in every lamella. This modulation may be attributed to the fact that the carbon-carbon bond lengths in graphite and alkyl chains are similar but not identical, which leads to repeat distances along the carbon chain of 246 pm and 254 pm, respectively. For a heptacosane ($C_{27}H_{56}$) molecule with 13 repeat units (two methylenes each), this mismatch adds up to 104 pm per molecule, which can be easily resolved by STM. In addition, it may be that the main molecular axis is tilted by a few degrees relative to the graphite axis. The images are, therefore, interpreted as moiré patterns between the linear carbon chain lattices of adsorbate and substrate.

The lack of discernible superstructure along the lamellae indicates that the unit cell of the adsorbate lattice contains one molecule in this direction and that it is commensurate with the substrate. The corresponding repeat unit in graphite is between the second from the next carbon rows and amounts to 426 pm, which is of the order of the width of an alkyl chain. More precisely, the intermolecular spacings in triclinic 3-D alkane crystals are about 420 and 480 pm in the directions perpendicular to and parallel with the carbon skeleton planes, respectively, as can be calculated from the x-ray structure data of octadecane (*21*). If the alkyl skeleton planes would be oriented parallel to the substrate as well as in registry with it, as has been proposed for another long-chain alkane (*20*) as well as for an alkyl derivative, octylcyanobiphenyl (*14*), it would require a compression of the monolayer by more than 10% compared to the bulk structure. However, the separation between perpendicularly oriented carbon skeleton planes agrees with the separation between the second from the next carbon rows in graphite. Because of the relatively weak interaction between the alkyl chains and graphite, we believe, therefore, that in alkane monolayers the carbon skeletons are oriented preferentially perpendicular to the graphite surface plane.

If, on the other hand, the head group of an alkyl derivative requires more space, then the alkyl carbon planes may lie flat. However, in this case the commensurability along the lamellae will be lost. An example is a monolayer of a fatty acid, whose STM image exhibits a superstructure along the lamellae with a repeat distance of about five alkyl chains (Fig. 1B). We attribute this to a mismatch between the flat-lying alkyl skeletons and the substrate lattice of about 10%, which means that for every five alkyl chains there is about one extra carbon row required in graphite.

Similarly, the alcohol (Fig. 1C) does not exhibit such a superstructure along the lamellae while the dialkylbenzene (Fig. 1D) does. In analogy to the alkane and the fatty acid (Fig. 1, A and B) the superstructure is attributed to a perpendicular and a parallel orientation of the carbon skeletons on the graphite surface, respectively. The alkyl chains form an angle of only 60° with the lamella boundaries, which implies that both the alkyl chains and the lamellae can be oriented parallel to a graphite axis. This allows the formation of molecularly defined domain boundaries of low energy, which occur between the three possible domain orientations according to the threefold symmetry of the graphite lattice. Because of the low energy associated with these domain boundaries, they are very abundant (*7, 19*). In fact, the domain sizes are typically not larger than a few tens of nanometers, whereas for the alkanes they can be as large as the single crystalline grains in the HOPG substrate, that is, on the order of a micrometer.

So far the molecular patterns have been treated as static, that is, image features have been attributed to the average positions of the molecules during the time required for an image recording. However, although the images displayed in Fig. 1 were stable for long times, occasionally some metastable defects do occur (*7, 19*). Also, the full reversibility of the adsorption (*10*) indicates considerable dynamics. Direct evidence for such mobility is given in Fig. 2, which displays three STM images of the same area of a monolayer of octadecanol, recorded at intervals of a few seconds. Several domains are shown in Fig. 2A, many of them exhibiting a herringbone structure as shown in Fig. 1C. The boundaries between the lamellar domains are molecularly defined. However, the part of the pattern at the upper left corner is not stable on the time scale of seconds, as evidenced by Fig. 2, B and C. Particularly interesting is the tilt-flip in the two vertical lamellae in the upper left corner. Because Fig. 2B was recorded from the bottom of the image to the top, the lower part is the old structure as in Fig. 2A and the upper part is the new one. From the sharpness of the transition from the old to the new structure and the scan speed, one can deduce that the flip occurred during not more than 10 ms. During that time the molecules in these particular lamellae have probably lifted, rearranged, and adsorbed again. The final configuration with two parallel vertical herringbones (Fig. 2C) appeared more stable, similar to the surrounding more perfect herringbone lamellae.

In conclusion, STM images of monolayers of long-chain alkanes and several simple alkyl derivatives on graphite are the result of (i) the contrast assignment to both substrate and adsorbate structure, and (ii) the different relative orientations and commensurabilities of the various adsorbates. All of the alkyl derivatives we investigated form well-ordered lamellae. However, although the carbon skeleton planes in the alkane and the alcohol are oriented preferentially perpendicular to the substrate, they lie predominantly flat in the fatty acid and didodecylbenzene. The consequences are adsorbate lattices, which are commensurate with the graphite in the one case and noncommensurate in the other. Most interesting is the mobility observed in phases, where the molecules are tilted relative to the lamella boundaries. In particular, the tilt-flip in individual lamellae of a length of a few nanometers could be observed on a time scale of a few milliseconds.

REFERENCES AND NOTES

1. R. J. Birgeneau and P. M. Horn, *Science* **232**, 329 (1986).
2. S. Garoff, H. W. Deckman, J. H. Dunsmuir, M. S. Alvarez, J. M. Bloch, *J. Phys. (Paris)* **47**, 701 (1986).
3. M. Seul, P. Eisenberger, H. M. McConnel, *Proc. Natl. Acad. Sci. U.S.A.* **80**, 5795 (1983).
4. R. M. Kenn *et al.*, *J. Phys. Chem.* **95**, 2092 (1991).
5. J. P. Rabe, J. D. Swalen, J. F. Rabolt, *J. Chem. Phys.* **86**, 1601 (1987).
6. G. Binnig and H. Rohrer, *IBM J. Res. Dev.* **30**, 355 (1986).
7. J. P. Rabe and S. Buchholz, *Phys. Rev. Lett.* **66**, 2096 (1991).
8. P. E. Laibinis, J. J. Hickman, M. S. Wrighton, G. M. Whitesides, *Science* **245**, 845 (1989).

9. A. J. Groszek, *Nature* 196, 531 (1962); *ibid.* 204, 680 (1964); *Proc. R. Soc. London Ser. A* 314, 473 (1970).
10. G. H. Findenegg and M. Lippard, *Carbon* 25, 119 (1987).
11. G. D. Parfitt and E. Willis, *J. Phys. Chem.* 68, 1780 (1964).
12. P. H. Lippel, R. J. Wilson, M. D. Miller, Ch. Wöll, S. Chiang, *Phys. Rev. Lett.* 62, 171 (1989).
13. J. K. Spong *et al.*, *Nature* 338, 137 (1989).
14. D. P. E. Smith, J. K. H. Hörber, G. Binnig, H. Nejoh, *ibid.* 344, 641 (1990).
15. W. Mizutani, M. Shigeno, M. Ono, K. Kajimura, *Appl. Phys. Lett.* 56, 1974 (1990).
16. H. Ohtani, R. J. Wilson, S. Chiang, C. M. Mate, *Phys. Rev. Lett.* 60, 2398 (1988).
17. R. Lazzaroni, A. Calderone, G. Lambin, J. P. Rabe, J. L. Brédas, *Synth. Metals* 41, 525 (1991).
18. J. P. Rabe, M. Sano, D. Batchelder, A. A. Kalatchev, *J. Microsc. (Oxford)* 152, 573 (1988).
19. S. Buchholz and J. P. Rabe, *J. Vac. Sci. Technol. B*, in press.
20. G. C. McGonigal, R. H. Bernhardt, D. J. Thomson, *Appl. Phys. Lett.* 57, 1 (1990).
21. A. I. Kitaigorodskij and J. B. Mnjukh, *Bull. Acad. Sci. U.S.S.R. Div. Chem. Sci.* (1959), p. 1992.
22. This project was supported by the Bundesministerium für Forschung und Technologie under the title "Ultrathin Polymer Layers" 03M4008E9 and the European Science Foundation (Additional Activity: Chemistry and Physics of Polymer Surfaces and Interfaces). S.B. acknowledges support through a Kekulé scholarship, granted by the Verband der Chemischen Industrie.

11 March 1991; accepted 29 May 1991

Dislocations and Flux Pinning in $YBa_2Cu_3O_{7-\delta}$

S. JIN, G. W. KAMMLOTT, S. NAKAHARA, T. H. TIEFEL, J. E. GRAEBNER

Bulk $YBa_2Cu_3O_{7-\delta}$ superconductors, under certain processing conditions such as melt texturing, exhibit a very high dislocation density of 10^9 to 10^{10} per square centimeter. In addition, the density of low-angle grain boundaries in such samples can be significantly increased (to less than ~700-nanometer spacing) through a dispersion of submicrometer-sized Y_2BaCuO_5 inclusions. These defect densities are comparable to those in high critical current thin films as revealed through scanning tunneling microscopy, and yet the critical current densities in the bulk materials (at 77 kelvin and a field of 1 tesla for example) remain at a 10^4 amperes per square centimeter level, about two orders of magnitude lower than in thin films. The results imply that these defect density levels are not significant enough to explain the difference in flux pinning strength between the thin film and bulk materials. The observation of spiral-like growth of the superconductor phase in bulk Y-Ba-Cu-O is also reported.

THE MAIN ADVANTAGE OF A SUPERconductor over a conventional conductor such as copper is the large amount of electrical current that it can carry by virtue of its zero resistance. Thus high current-carrying capability is essential for major bulk applications of the new, high transition temperature (T_c) superconductors. Epitaxial thin films of the high T_c superconductor $YBa_2Cu_3O_{7-\delta}$ typically exhibit high critical current densities (J_c) in excess of 10^6 A cm^{-2} at 77 K even in the presence of strong magnetic fields. The bulk materials, on the other hand, have about two orders of magnitude lower J_c (~10^4 A cm^{-2}).

Hawley *et al.* (*1*) and Gerber *et al.* (*2*) have recently observed, through scanning tunneling microscopy, a high density of screw dislocations (~10^9 cm^{-2}) associated with spiral growth in epitaxial thin films of Y-Ba-Cu-O. They discuss the possibility of flux pinning by the observed screw dislocations (and the defects in low angle grain boundaries between the spirals), and suggest that the high dislocation density may be related to the significantly higher J_c in thin films than in bulk materials. We report here the observation of a comparably high density of dislocations in some bulk Y-Ba-Cu-O superconductors and discuss the possible relationship of the defects to the flux pinning behavior in bulk and thin film superconductors.

Bulk $YBa_2Cu_3O_{7-\delta}$ samples ("123" phase) were prepared in three different forms; sintered pellets (940°C for 40 hours in O_2 and furnace cool), sintered ribbons (~6-μm-thick $YBa_2Cu_3O_{7-\delta}$ on ~12-μm-thick silver substrate by spray coating of powder, cold rolling by ~90% reduction in cross-sectional area, and sintering at 940°C for 100 hours in O_2 and furnace cool), and locally melt-textured bars (continuous cooling, in the absence of temperature gradient, from ~1050° to 380°C at 2° to 10°C per hour in O_2).

The dispersion of fine Y_2BaCuO_5 inclusions ("211" phase) was made by melt-texture processing of off-stoichiometric samples containing a fine-scale compositional segregation richer in Y and Ba (*3*, *4*). The resultant samples contained about 30 to 45 vol. % of submicrometer-sized "211" particles in "123" matrix. All the samples exhibited T_c ($R = 0$) > 90 K and T_c (midpoint) by ac susceptibility measurement of 90 to 95K.

Transmission electron microscopy (TEM) for the analysis of dislocations in Y-Ba-Cu-O (*5*) was carried out using a Philips 430 electron microscope operated at 300 kV. Scanning electron microscopy (SEM) was conducted at 20 kV. Magnetization measurements (*M-H* hysteresis loops) were made at 77 K with a vibrating sample magnetometer using a sweep rate of ~80 Oe s^{-1} and the maximum applied field of ±9 T. The intragranular J_c (which is proportional to flux pinning strength) was estimated from the *M-H* loop by using the Bean model (*6*). The average grain diameter based on high-angle boundaries was used as the size of the supercurrent loop, as it is well established that low-angle grain boundaries in Y-Ba-Cu-O are not weak links.

The TEM micrograph for the melt-textured sample (Fig. 1) shows an example of a high density of dislocations estimated to be in excess of 10^9 cm^{-2}. This is in sharp contrast to the sintered samples which typically contain relatively few dislocations (10^6 to 10^7 cm^{-2}). The exact cause for the increased number of dislocations in melt-textured Y-Ba-Cu-O is not clearly understood, but it may be related to a number of factors such as (i) the accommodation, during crystal growth below 1000°C, of lattice parameter changes in the presence of local cation concentration gradient, (ii) the relief of internal stresses caused by local temperature gradient, (iii) the strains associated with the merger of parallel "123" plates with slight misorientations, (iv) the strains caused by bending and forced merger of neighboring "123" plates as the trapped $BaCuO_2$ or CuO phase between them is removed by diffusion or evaporation (a 10 to 30% decrease in weight is common in melt-texture processing owing to the partial loss of BaO and

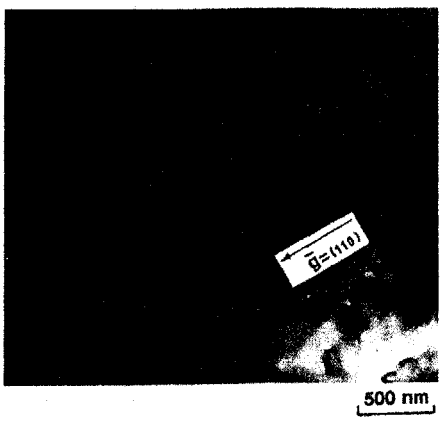

Fig. 1. TEM micrograph showing dislocations in melt-textured Y-Ba-Cu-O.

AT&T Bell Laboratories, Murray Hill, NJ 07974.